ADVANCED MATERIALS
www.advmat.de

Synthesis of 2D Porous Crystalline Materials in Simulated Microgravity

Noemí Contreras-Pereda, David Rodríguez-San-Miguel, Carlos Franco, Semih Sevim, João Pedro Vale, Eduardo Solano, Wye-Khay Fong, Alessandra Del Giudice, Luciano Galantini, Raphael Pfattner, Salvador Pané, Tiago Sotto Mayor,* Daniel Ruiz-Molina,* and Josep Puigmartí-Luis**

To date, crystallization studies conducted in space laboratories, which are prohibitively costly and unsuitable to most research laboratories, have shown the valuable effects of microgravity during crystal growth and morphogenesis. Herein, an easy and highly efficient method is shown to achieve space-like experimentation conditions on Earth employing custom-made microfluidic devices to fabricate 2D porous crystalline molecular frameworks. It is confirmed that experimentation under these simulated microgravity conditions has unprecedented effects on the orientation, compactness and crack-free generation of 2D porous crystalline molecular frameworks as well as in their integration and crystal morphogenesis. It is believed that this work will provide a new "playground" to chemists, physicists, and materials scientists that desire to process unprecedented 2D functional materials and devices.

1. Introduction

Reactions are frequently conducted under vigorous stirring to improve the mass transport of reagents and to increase the reaction efficiency via turbulent flows. However, turbulent conditions lead to a poor control of convective transport processes which may prompt the precipitation of reaction products and significantly affect the reaction performance. This scenario is especially critical during the synthesis of 2D and 3D functional crystals with controlled sizes and shapes. For example, 3D crystalline porous molecular frameworks such as metal–organic frameworks (MOFs) are often synthesized using turbulent mixing,[1] and/or solvothermal methods,[2,3] among others.[4] In these synthetic conditions, the formation of MOF crystals depletes the surrounding monomer solution, thus creating buoyancy-driven convection, which generates uneven growth rates and the precipitation (sedimentation) of crystals in solution. Precipitation can significantly affect the reaction performance, for example, by leading to a non-controlled and non-uniform

N. Contreras-Pereda, Dr. D. Ruiz-Molina
Catalan Institute of Nanoscience and Nanotechnology (ICN2)
CSIC and BIST
Campus UAB
Bellaterra
Barcelona 08193, Spain
E-mail: dani.ruiz@icn2.cat

Dr. D. Rodríguez-San-Miguel, Dr. C. Franco, S. Sevim
Department of Chemistry and Applied Biosciences
Institute for Chemical and Bioengineering
ETH Zurich
Zurich 8093, Switzerland

Dr. D. Rodríguez-San-Miguel, Prof. J. Puigmartí-Luis
Departament de Ciència dels Materials i Química Física
Institut de Química Teòrica i Computacional
Barcelona 08028, Spain
E-mail: josep.puigmarti@ub.edu

J. P. Vale, Dr. T. S. Mayor
SIMTECH Laboratory
Transport Phenomena Research Centre
Engineering Faculty of Porto University
Porto 4200–465, Portugal
E-mail: tiago.sottomayor@fe.up.pt

The ORCID identification number(s) for the author(s) of this article can be found under https://doi.org/10.1002/adma.202101777.

Dr. E. Solano
ALBA Synchrotron
Carrer de la Llum 2–26
Cerdanyola del Vallès, Barcelona 08290, Spain

Prof. W.-K. Fong
Discipline of Chemistry
School of Environmental and Life Sciences
University of Newcastle
Callaghan, NSW 2308, Australia

Dr. A. D. Giudice, Prof. L. Galantini
Department of Chemistry
Sapienza University of Rome
P. le A. Moro 5, Rome 00185, Italy

Dr. R. Pfattner
Institut de Ciència de Materials de Barcelona
ICMAB-CSIC
Campus UAB, Bellaterra 08193, Spain
E-mail: rpfattner@icmab.es

Prof. S. Pané
Multi-Scale Robotics Lab
ETH Zurich
Tannenstrasse 3, Zurich CH-8092, Switzerland

Prof. J. Puigmartí-Luis
ICREA
Pg. Lluís Companys 23, Barcelona 08010, Spain

DOI: 10.1002/adma.202101777

growth rate of MOF crystals in solution. Other methods that are particularly suitable for the generation of functional 2D porous crystalline molecular frameworks (e.g., 2D MOFs) are surface-templated growth methods[5,6] or interfacial synthetic approaches (e.g., liquid/air or liquid/liquid interfaces).[7–9] Certainly, these methods can also suffer non-controlled convective transport processes (e.g., surface-tension-driven convection (Marangoni convection)) and precipitation leading to fragmentation of the MOF films as well as to a poor control over their orientation, compactness, roughness profile, and/or morphology, features that greatly impact their function and performance.[7,8]

Recently, groundbreaking studies at the International Space Station clearly confirmed the favorable effect of microgravity on the growth of crystalline matter.[10] It has been demonstrated that the convection-free mass transport occurring in microgravity conditions can greatly favor the synthesis of materials with larger crystalline domain sizes, lower defect densities and new morphologies.[11] However, the high costs and restricted access to experimentation in space have hindered efforts to study and control the engineering of crystalline porous molecular frameworks under these synthetic conditions. Herein, we show that microfluidic devices can simulate on Earth the effect of the microgravity in space experimentation. Then, we use this microfluidic approach to control the synthesis and growth of a prototypal conductive 2D MOF, i.e., $Ni_3(HITP)_2$ (where HITP stands for 2, 3, 6, 7, 10, 11-hexaiminotriphenylene). We observe the formation of defect-free centimeter-sized thin films of $Ni_3(HITP)_2$ that exhibit conductivities of up to 40 S cm^{-1} over large distances at ambient conditions. Note that, thus far, similar values outside of an inert atmosphere have only been achieved with pellets prepared under high pressures (≈1 GPa).[12]

We chose $Ni_3(HITP)_2$ as an exemplar case for three main reasons: i) $Ni_3(HITP)_2$ is a MOF whose growth has been difficult to control as it quickly precipitates from the reaction media as black particles under alkaline media and an uncontrolled atmospheric oxygen diffusion.[13] ii) $Ni_3(HITP)_2$ is a conductive 2D MOF with extended π-conjugation, analogous to graphene, but whose conductivity properties have been derived mainly from pressed pellets and from polycrystalline $Ni_3(HITP)_2$ powder but not in defect-free thin-films.[14] iii) $Ni_3(HITP)_2$ is synthetized following a two-step vapor induced crystallization approach, first with volatile alkaline vapors and subsequently with oxidant gases, that cannot be systematically controlled employing common synthetic approaches.[7]

2. Results and Discussion

First, we engineered a microfluidic device that consists of two substrates sandwiched with a thin silicone film with variable thicknesses (from 200 to 500 µm) to create a microfluidic environment that is 6 cm long and 1.5 cm wide (see **Figure 1**a and Section S3 in the Supporting Information for further details). One of the surfaces has two machined inlet ports that allow for the injection and complete filling of the microfluidic environment preventing the appearance of air bubbles (Figure 1b,c). We believe that the environment created between the two substrates can simulate space experimentation where the synthesis of $Ni_3(HITP)_2$ can be accomplished in the absence of buoyancy-driven convection. This belief is clearly supported by numerical simulations of the transport phenomena inside the microfluidic device (see Section S4 in the Supporting Information for further details). Two scenarios were considered in our numerical analyses: i) the conventionally used vapor-assisted conversion method,[15] where $Ni_3(HITP)_2$ is generated from a hypothetical droplet of precursors when exposed to volatile alkaline gas and atmospheric oxygen, and ii) the synthesis of $Ni_3(HITP)_2$ inside our custom-made microfluidic device, where a controlled diffusion of the volatile reactive species in the static reaction media can be easily achieved. The microfluidic device was assumed to be filled with the dimethylsulfoxide (DMSO) solution of $Ni_3(HITP)_2$ precursors, and then the gases were allowed to diffuse through the gas-liquid interface at the inlets.

Interestingly, we observed that in the droplet scenario, there are two counter-rotating vortices spanning most of the droplet diameter (see Figure 1d), where fluid elements move inward along the droplet upper free surface (i.e., the gas-liquid interface) and outward near the substrate. In agreement with this, there is an evident accumulation of the less dense solute in the upper part of the droplet (Figure 1f), and a horizontal concentration front moving downward toward the substrate (i.e., in the direction of gravity), see Figure 1f. In this scenario, the precursors can mix and react in the upper part of the droplet, before the solute concentration front reaches the substrate. During this time, $Ni_3(HITP)_2$ powders may start to form in the upper part of the droplet due to the oxidation reaction with atmospheric oxygen, and the $Ni_3(HITP)_2$ precipitate will be pulled down by gravity, adding to the already existing convective currents inside the droplet. In sharp contrast, and as shown in Figure 1e, the microfluidic device used in our investigations allows for the dramatic reduction of the convective mass transport effect during the reaction process. Indeed, much smaller/weaker vortices are observed (and only near the device inlets), whose velocities (in the µm s^{-1} range) are ≈1000 times smaller (at 1 min) and ≈25 smaller (at 30 min) than those observed inside the droplet (see Figure 1d and Figure S5 (Supporting Information), respectively). In agreement with this, the concentration profile is also vastly different from that in the droplet scenario, with the microfluidic device generating a vertical concentration front moving horizontally along the substrate length (i.e., perpendicular to the direction of gravity), see Figure 1g. The clearly different synthetic conditions generated with our microfluidic approach enables the vapor-assisted synthesis of $Ni_3(HITP)_2$ in a reaction environment that guarantees the convection-free mass transport conditions achieved in space experimentation. Note that a microfluidic device as thick as the droplet also generates horizontal concentration fronts inside reaction media, see Figures S6 and S7 (Supporting Information). Even though other microfluidic devices have been used to synthesize MOF crystals,[16–18] to date none of these microfluidic methods are capable of generating vertical concentration fronts that move horizontally along a substrate employing gases as reagents.

In order to experimentally confirm the controlled two-step vapor induced crystallization of $Ni_3(HITP)_2$ inside our microfluidic environment, we firstly assembled the microfluidic device with two quartz slides as top and bottom walls (Figure 1a). This

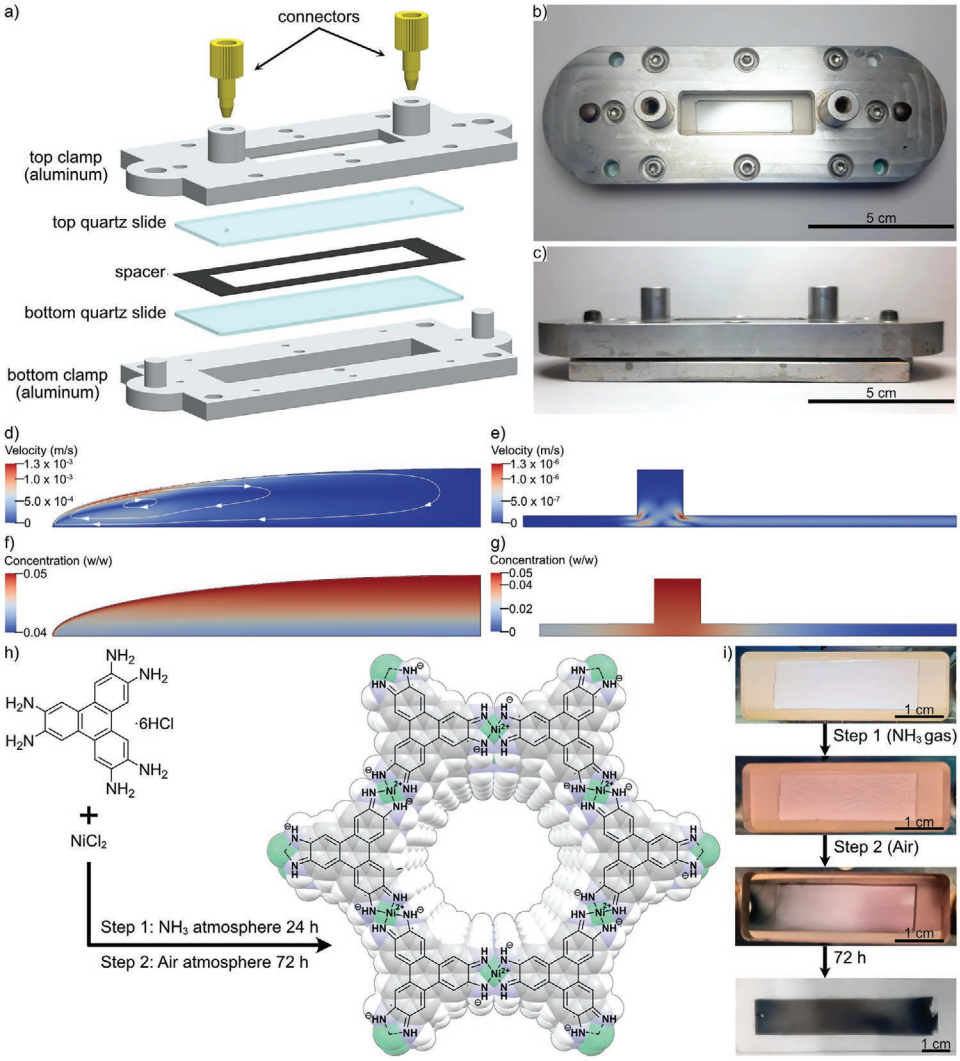

Figure 1. a) Illustration showing an expanded view of the microfluidic device. b,c) Top and side view photographs of the microfluidic device, respectively. d,e) Velocity maps after 1 min of simulation time for the droplet and the microfluidic device, respectively. The images are zoomed in to allow the visualization of the flow details. Streamlines are also shown in the droplet velocity map to highlight the motion of the fluid elements. The velocity range in the droplet is ≈1000 times larger than that in the microfluidic device. f,g) Concentration maps after 30 min of simulation time for the droplet and the microfluidic device, respectively. The concentration maps are shown with ranges of 0.04–0.05 w/w and 0–0.05 w/w, respectively. h) Schematic illustration of the synthetic pathway followed to obtain $Ni_3(HITP)_2$. i) Photographs of the microfluidic environment at the different stages during the synthesis of $Ni_3(HITP)_2$. The initial colorless solution becomes pink upon exposure to ammonia vapors for 24 h, i.e., step 1. In step 2, the pink solution progressively becomes black from the inlets toward the center of the chamber upon exposure to air. After 72 h, a black thin film supported on quartz can be observed.

configuration was preferred as it enables following the reaction progress of $Ni_3(HITP)_2$ both optically and spectroscopically. Anhydrous DMSO was chosen as the solvent of reaction. DMSO can solubilize all the reactants ($NiCl_2$ and HATP·6HCl, where HATP stands for 2,3,6,7,10,11-hexaaminotriphenylene), including intermediate species, thus preventing nucleation and growth of $Ni_3(HITP)_2$ by avoiding the movement of precipitates inside the microfluidic device. The microfluidic device was first filled with the solution of the reactants; next, the two-step vapor induced crystallization approach of $Ni_3(HITP)_2$ (Figure 1h) was accomplished by controlling the diffusion of ammonia gas (step 1) and air (step 2) inside the microfluidic device through its inlets (see the Supporting Information for further details). As shown in Figure 1i, the initially colorless solution composed by a stoichiometric mixture of $NiCl_2$ and HATP·6HCl turns pink during step 1, i.e., when the microfluidic device is introduced in a chamber full of ammonia vapor for 24 h. Subsequently, this pink solution turns black at the inlet ports in step 2, i.e., upon exposure to air. After 72 h, the substrate is completely covered with a black film that can readily be analyzed as $Ni_3(HITP)_2$, see Figure 1i. The UV–vis spectra in Figure S11 (Supporting Information) clearly show these color changes. An intense absorption band at 1000 nm corresponding to the non-oxidized complex between non-protonated HATP and the metal cation is detected right after taking the device out of the ammonia atmosphere. Then, when the device is exposed to air, the band

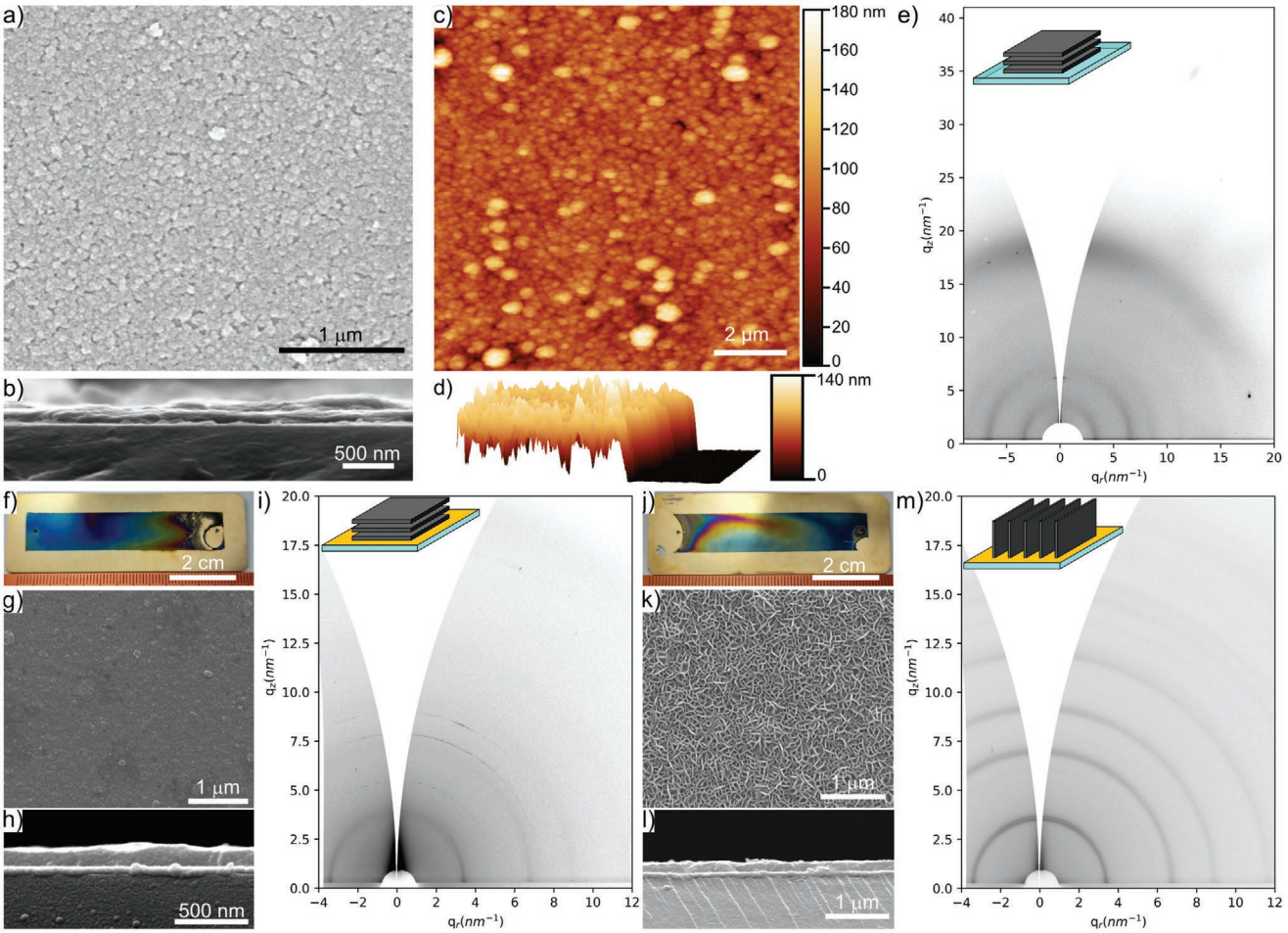

Figure 2. a) Top-view SEM image of a $Ni_3(HITP)_2$@Quartz film. b) Cross-section SEM image of a $Ni_3(HITP)_2$@Quartz film. c) AFM image of a $Ni_3(HITP)_2$@Quartz film. d) 3D AFM image of the edge of a $Ni_3(HITP)_2$@Quartz film. e) 2D GIWAXS pattern of a $Ni_3(HITP)_2$@Quartz film. The inset shows a scheme of the orientation of the $Ni_3(HITP)_2$@Quartz film. f) Optical photograph of a $Ni_3(HITP)_2$@Au film. g) Top-view SEM image of a $Ni_3(HITP)_2$@Au film. h) Cross-section SEM image of a $Ni_3(HITP)_2$@Au film. i) 2D GIWAXS pattern of a $Ni_3(HITP)_2$@Au film. The inset shows a scheme of the orientation of the $Ni_3(HITP)_2$@Au film. j) Optical photograph of a $Ni_3(HITP)_2$@Au-SAM film. k) Top-view SEM image of $Ni_3(HITP)_2$@Au-SAM film. l) Cross-section SEM image of a $Ni_3(HITP)_2$@Au-SAM film. m) 2D GIWAXS pattern of a $Ni_3(HITP)_2$@Au-SAM film. The inset shows a scheme of the orientation of the $Ni_3(HITP)_2$@Au-SAM film.

at 1000 nm starts to decrease while the characteristic band of $Ni_3(HITP)_2$ at 530 nm appears and increases as the film is formed.[19] In contrast to this controlled two-step vapor induced crystallization of $Ni_3(HITP)_2$ inside the microfluidic device, performing the same reaction in bulk conditions (e.g., in a vial) results in a fast precipitation of black particles at the air/DMSO interface characterized as $Ni_3(HITP)_2$ (see Section S5 in the Supporting Information). In this case, monitoring the reaction by UV–vis spectroscopy (Figure S10, Supporting Information) does not allow to identify the non-oxidized pink intermediate, since the band at 530 nm is present from the first spectrum and the band at 1000 nm has already decreased its intensity considerably right after the addition of the base. This rapid progress of the reaction in bulk, without the appearance of the two distinct stages, showcases the lack of control over the oxygen diffusion when conventional synthetic conditions are in place.

The black $Ni_3(HITP)_2$ films supported on quartz (here after referred to as $Ni_3(HITP)_2$@Quartz films) were initially characterized by scanning electron microscopy (SEM), which revealed a smooth, compact and crack-free continuous film with a homogeneous thickness of 100 nm (**Figure 2**a,b), that was further confirmed by profilometry (Figure 2d). Atomic force microscopy (AFM) confirmed the low roughness of the film where a root mean square (RMS) roughness of 14.9 ± 0.5 nm was measured (Figure 2c). The crystallinity and structure of the $Ni_3(HITP)_2$@Quartz films were assessed by 2D grazing-incidence wide-angle X-ray scattering (GIWAXS). The reflections corresponding to the $Ni_3(HITP)_2$ structure at $q_r = 3.4$ nm^{-1} (100), $q_r = 6.7$ nm^{-1} (200), $q_r = 8.9$ nm^{-1} (130), $q_r = 11.7$ nm^{-1} (240), and $q_z \approx 18$ nm^{-1} (002) are clearly observed in Figure 2e, where they appear with an anisotropic distribution.[19] That is, plotting the intensities in an azimuthal representation (Figure S12, Supporting Information) clearly shows that the (*hk*0) peaks have higher intensity in the in-plane direction, while the (002) peak is mainly localized in the out-of-plane direction. These data suggest that the $Ni_3(HITP)_2$ structure is preferentially oriented with its *c*-axis perpendicular to the substrate. As shown in Figure S13 (Supporting Information), the

layers of $Ni_3(HITP)_2$ extend through coordination bonds along the a and b axes and are separated by a typical π–π stacking distance of 0.33 nm along the *c*-axis. Accordingly, and based on the unit cell of $Ni_3(HITP)_2$, the GIWAXS data indicates that the layers of the MOF in $Ni_3(HITP)_2$@Quartz films have grown parallel to the quartz surface. It is worth noting that if a quartz substrate is immersed in a vial containing the same reaction mixture (in the presence of buoyancy-driven convection), $Ni_3(HITP)_2$ can be generated but the resulting coverage of the substrate is not compact nor homogeneous. Additionally, in this case, the $Ni_3(HITP)_2$ films produced do not have a preferential orientation (Figure S14, Supporting Information). These results clearly highlight the importance of avoiding convective mass transport during the synthesis of $Ni_3(HITP)_2$ thin films. Undoubtedly, with our microfluidic device, we allow the growth of $Ni_3(HITP)_2$ in a quiescent environment that ensures the generation of compact, smooth and crack-free $Ni_3(HITP)_2$ thin films.

Since $Ni_3(HITP)_2$ is a promising conductive material that will have to be interfaced with electrodes in order to build functional devices, we extended our synthetic microfluidic approach to gold substrates. The use of gold was twofold: i) On the one hand, it provides a conductive surface to analyze the electronic properties of the as-prepared $Ni_3(HITP)_2$ thin films. On the other hand, ii) it facilitates the rational surface engineering of the microfluidic environment. Gold can be readily functionalized with thiols, forming self-assembled monolayers (SAMs), a feature that can be exploited to trigger a controlled orientation of $Ni_3(HITP)_2$ films during their growth in the simulated microgravity conditions achieved with our microfluidic device.

As shown in Figure 2f, assembling the microfluidic device with two glass slides sputtered with gold as top and bottom walls and performing the synthesis of $Ni_3(HITP)_2$ as indicated above, yielded a large centimeter-scale $Ni_3(HITP)_2$ film, hereafter called $Ni_3(HITP)_2$@Au film. The morphology of the $Ni_3(HITP)_2$@Au films is again compact, smooth and crack-free with a thickness of ≈100 nm (Figure 2g,h). HR-TEM of the material removed from $Ni_3(HITP)_2$@Au films shows the high quality of the $Ni_3(HITP)_2$ crystals generated, in which the interlayer distance of 0.33 nm can be observed directly from the images, while selected area electron diffraction (SAED) patterns show peaks matching the (100) and (200) crystallographic planes (Figure S15, Supporting Information). Finally, the 2D GIWAXS images are very similar to those reported for $Ni_3(HITP)_2$@Quartz films, with the (*hk*0) peaks displaying a higher intensity in the in-plane direction, indicating that $Ni_3(HITP)_2$@Au films are also preferentially oriented with the *c*-axis perpendicular to the substrate (Figure 2i and Figure S16: Supporting Information).

Next, we decided to functionalize the gold surface with an amino-terminated SAM (see Section S7 in the Supporting Information for further details) to study if the nature of the substrate with the presence of anchoring groups can have some influence over the growth of $Ni_3(HITP)_2$ when a convection-free mass transport condition is achieved. Note that gold surfaces functionalized with chemical groups mimicking those of linkers have been used to grow conductive 2D MOFs under convective mass transport processes and employing a layer-by-layer approach.[20] Therefore, the amino groups of our SAM are expected to have strong directional interactions with the building blocks of $Ni_3(HITP)_2$, either by coordination to the nickel cations or through hydrogen bonds with the ligand. Accordingly, a completely different microfluidic-based synthetic environment was designed in these studies to perform the two-step vapor induced crystallization of $Ni_3(HITP)_2$ films under the convection-free mass transport condition achieved in our microfluidic device when compared to the film grown onto bare gold and quartz substrates.

Even though the films grown on bare gold and on Au-SAMs substrates looked similar to the naked eye (Figure 2f,j, respectively), the $Ni_3(HITP)_2$@Au-SAM films showed a very different morphology when observed by SEM. As shown in Figure 2k,l, the $Ni_3(HITP)_2$@Au-SAM films consist of densely packed nanoplatelets attached edge-on to the Au-SAM substrate, while the thickness remains at ≈100 nm. This striking morphological change was also corroborated by AFM, which also allowed to assess the significant difference in roughness between $Ni_3(HITP)_2$@Au and $Ni_3(HITP)_2$@Au-SAM films (Figures S17 and S18: Supporting Information). From the AFM images, the RMS of $Ni_3(HITP)_2$@Au films is 7.2 ± 0.5 nm while the RMS for $Ni_3(HITP)_2$@Au-SAM films is 24.1 ± 0.6 nm. More interestingly, 2D GIWAXS measurements showed that this morphological change arises from a change in the orientation of the $Ni_3(HITP)_2$ crystals generated. As seen in Figure 2m and Figure S19 (Supporting Information), the (*hk*0) peaks acquired from the 2D GIWAXS patterns of $Ni_3(HITP)_2$@Au-SAM films are more intense in the out-of-plane direction, which is in agreement with a preferential orientation of the $Ni_3(HITP)_2$@Au-SAM films with the *c*-axis parallel to the substrate. These results are in sharp contrast to earlier observations where $Ni_3(HITP)_2$@Au films were grown with a preferred orientation of the *c*-axis perpendicular to the substrate. HR-TEM images of the material removed from $Ni_3(HITP)_2$@Au-SAM films reveal hexagonal patterns with periodicities of 2 nm, matching the pores of the $Ni_3(HITP)_2$ structure. Additionally, SAED patterns also show the (100) and (200) reflections of $Ni_3(HITP)_2$ crystals as for $Ni_3(HITP)_2$@Au films (Figure S20, Supporting Information). Altogether, these results show the versatility of our approach for the preparation of compact and crack-free $Ni_3(HITP)_2$ thin films both in conductive and insulating substrates, i.e., on quartz and/or gold substrates, respectively. Strikingly, it was also demonstrated that the simulated microgravity conditions achieved with our microfluidic device can trigger the growth of compact, smooth and crack-free $Ni_3(HITP)_2$ thin films with controlled preferred orientations, either perpendicular or parallel to the substrate, avoiding time-consuming, labor-intensive layer-by-layer approaches where fluid flow conditions are not controlled.

Since the $Ni_3(HITP)_2$ films have the same crystallographic orientation on quartz and gold, a microfluidic device assembled with quartz slides sputtered with gold electrodes was considered as the best case scenario to study the electrical anisotropy of the $Ni_3(HITP)_2$ films generated (**Figure 3**). Accordingly, quartz substrates with pre-patterned gold electrodes were used to grow $Ni_3(HITP)_2$@Electrodes films with their *c*-axis perpendicular to the substrate (Figure 3a,d). This electrode configuration, represented as geometry (i) in Figure 3b, allowed the direct characterization of the in-plane conductivity of $Ni_3(HITP)_2$@Electrodes films right after their generation

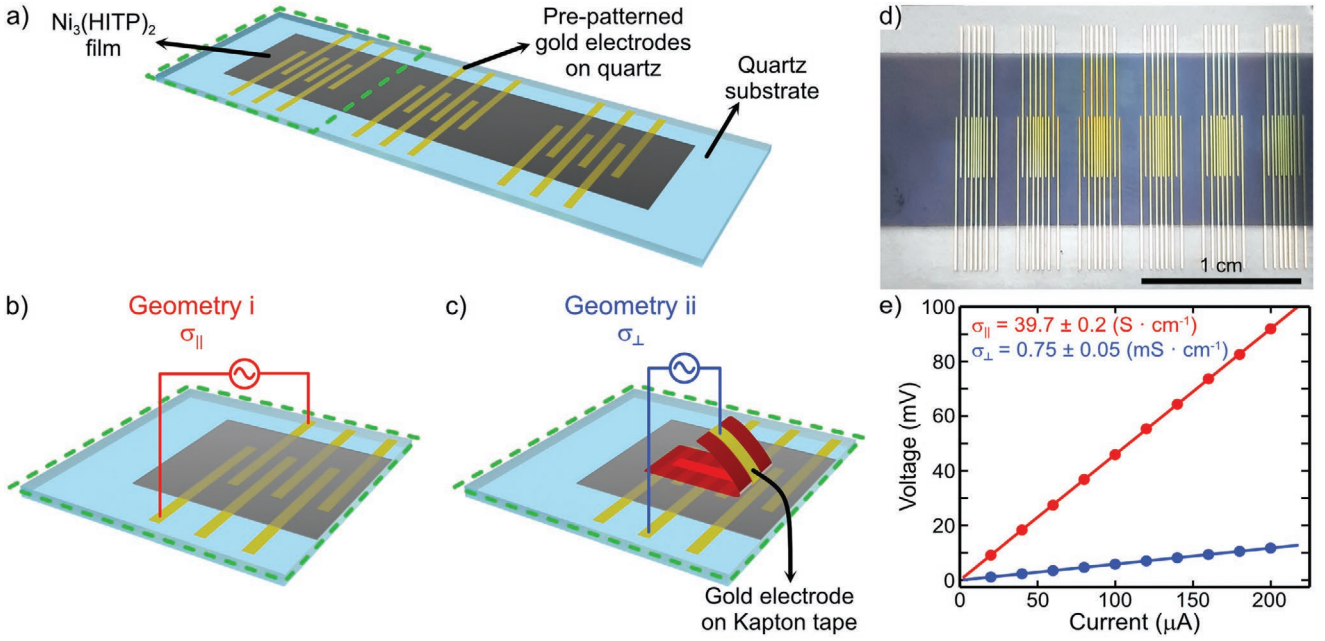

Figure 3. a) $Ni_3(HITP)_2$@Electrodes film (dark region in the center) grown on top of pre-patterned gold electrodes deposited by sputtering on a quartz substrate. b,c) Schematic views of the area highlighted in green in (A) showing the contact geometries employed to measure the electrical anisotropy of a $Ni_3(HITP)_2$@Electrodes film. b) Shows the contact used for in-plane conductivity, while (c) shows the gold contact thermally evaporated on a polyimide substrate and subsequentially pressed on top of the sample to measure the out-of-plane conductivity. d) $Ni_3(HITP)_2$@Electrodes film (dark region in the center) grown on top of pre-patterned gold electrodes deposited by sputtering on a quartz substrate, analogously to the scheme in (a). e) Lock-in AC *V*–*I* measurements of a $Ni_3(HITP)_2$@Electrodes film measured in-plane (red, geometry (i)) and vertical directions (blue, geometry (ii)).

inside our microfluidic device. However, the out-of-plane conductivity properties of $Ni_3(HITP)_2$@Electrodes films required a second set of electrodes on top of the $Ni_3(HITP)_2$@Electrodes films. Taking into account that the thermal evaporation or the sputtering of top electrode contacts onto the generated $Ni_3(HITP)_2$@Electrodes films will facilitate the intercalation of metal atoms into the film altering its electrical properties and eventually leading to electrical shortcuts, we conducted a different approach.[21] First, 50 nm of gold were thermally evaporated on polyimide substrates and these were mechanically transferred on top of the 100 nm-thick $Ni_3(HITP)_2$@Electrodes films, resulting in the contact geometry (ii) shown schematically in Figure 3c. These geometries allowed for the characterization of two relevant charge transport channels in the as-synthesized $Ni_3(HITP)_2$@Electrodes films. While geometry (i) allowed for the study of the in-plane charge transport (i.e., $\sigma_{\parallel}$), i.e., along the $Ni_3(HITP)_2$@Electrodes films, geometry (ii) gives access to out-of-plane charge transport ($\sigma_{\perp}$), i.e., perpendicular to the $Ni_3(HITP)_2$@Electrodes films. Performing this out-of-plane measurement through the extremely thin $Ni_3(HITP)_2$@Electrodes films is challenging using standard direct current (DC) measurement techniques because of the non-negligible contribution of contact resistances, so a Lock-in amplifier in A-B mode was used to efficiently filter DC contact voltages (see Figure S23 (Supporting Information) for calibration of the method). As shown in Figure 3e, the *V*–*I* plots obtained for both geometries are highly linear, which indicates good ohmic contacts[22] and negligible Fermi level pinning[23] along all directions of the $Ni_3(HITP)_2$@Electrodes films. Moreover, the phase during the measurements remains close to zero, showcasing negligible capacitive coupling in both geometries (Figure S24, Supporting Information). Linear fits of the *V*–*I* plots provided high conductivities of 39.7 ± 0.2 S cm^{-1}. Electrical conductivity measurements at different temperatures indicate an in-plane activation energy (E_a) of 64 ± 1 meV. A clear Arrhenius-type thermally activated transport with a very small thermal hysteresis was obtained for in-plane measurements under ambient pressure (see Figures S26 and S27 in the Supporting Information). Interestingly, such high conductivities close to 40 S cm^{-1} in triphenylene-based MOFs are normally only obtained under inert atmosphere or vacuum rather than in ambient conditions (see Table S2 in the Supporting Information), as water uptake diminishes the conductivity.[24] Furthermore, note that, at ambient conditions, only pelletization at high pressures (≈1 GPa)[12] has proved efficient to generate similar conductivities. Again, these results clearly showcase the good packing of $Ni_3(HITP)_2$ obtained with our microfluidic approach. On the other hand, the out-of-plane conductivity obtained from geometry (ii) is 0.75 ± 0.05 mS cm^{-1} with a corresponding activation energy of E_a = 121 ± 13 meV (Figure 3e and Figure S26: Supporting Information, respectively), which leads to a high anisotropy factor of more than 5×10^4. Similar high anisotropy factors have only been reported for graphite so far.[25–27] To ensure an optimal contact and the quality of the data obtained with the geometry (ii), we conducted additional out-of-plane *V*–*I* measurements using polyimide substrates that incorporated gold contacts with different areas. Remarkably, same values on the vertical conductivity were obtained (0.78 ± 0.05 mS cm^{-1}), thus confirming the validity of our measurements (Figure S27, Supporting Information).

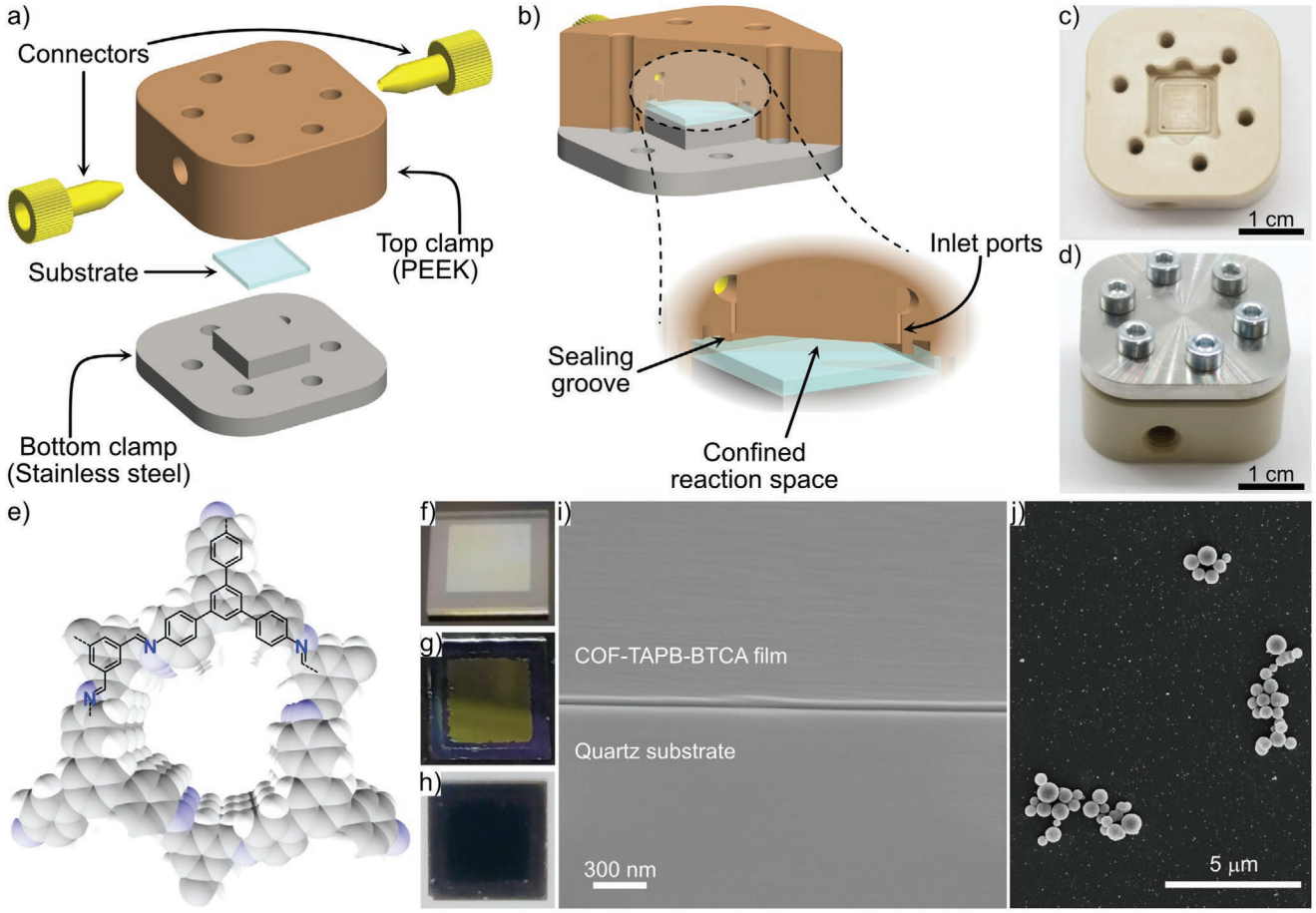

Figure 4. a,b) Illustrations showing expanded views of the microfluidic device. c) Top view photograph of the PEEK clamp (top clamp), showing the square sealing groove defining the confined reaction space. d) Side view photograph of the assembled microfluidic device, showing one of the ports for the connectors. e) Scheme of the structure of COF-TAPB-BTCA overlaid on a spacefill model of the structure. f–h) Optical photographs of COF-TAPB-BTCA films grown on 1 cm × 1 cm quartz (001), graphene and silicon (111) substrates, respectively. i) Side view SEM image of a thin film of COF-TAPB-BTCA grown on quartz (001). j) SEM image of COF-TAPB-BTCA synthesized onto a quartz surface immersed in the reaction mixture prepared in a vial.

To assess the generality of our approach, we also investigated the effect of the simulated microgravity conditions during the synthesis of COF-TAPB-BTCA, a well-known porous and crystalline 2D covalent organic framework (COF) resulting from the Schiff-base reaction between 1,3,5-tris(4-aminophenyl)benzene (TAPB) and 1,3,5-benzenetricarbaldehyde (BTCA), see **Figure 4**e.[28] In sharp contrast to $Ni_3(HITP)_2$, COF-TAPB-BTCA is now generated via covalent bonds instead of ionic interactions. Briefly, we initially chose acetone as a solvent since it completely dissolves TAPB and BTCA, and further, it avoids the fast precipitation of COF-TAPB-BTCA inside the microfluidic device. Accordingly, we designed a new solvent-resistant microfluidic device that can also accommodate a large variety of commercially and technologically relevant surfaces with a standard 1 cm × 1 cm size (e.g., silicon (111) and/or graphene). This new microfluidic device consists of a piece with a cavity in which the commercial surface is placed (see Figure 4a (top clamp) and Figure 4c). Then, the bottom clamp is clamped pressing the surface against a 200 μm-thick sealing groove to create the microfluidic environment presented in Figure 1g (Figure 4a–d and Section S9 in the Supporting Information). Note that the dimensions achieved with this new microfluidic device enable to keep the reduced convection benefits of the previous larger version (see Section S4 in the Supporting Information). When carrying out the synthesis of COF-TAPB-BTCA inside the new microfluidic device and using a quartz surface, an extremely smooth thin film was obtained 24 h after loading the reaction mixture in the cell (Figure 4f). See for example the SEM image of the COF-TAPB-BTCA film generated in Figure 4i or Figure S29 (Supporting Information). Further, we characterized the morphology of the COF-TAPB-BTCA films by AFM (Figure S30, Supporting Information). The data collected shows that defect-free centimeter-sized COF-TAPB-BTCA films as thin as 60 nm and with an extremely low roughness (RMS = 2.4 nm) can be prepared with our microfluidic device. Indeed, annealed films[29] show the characteristic GIWAXS pattern of COF-TAPB-BTCA with peaks at 4.1, 7.5, and 8.5 nm^{-1} corresponding to the (100), (200), and (110) reflections, respectively. Additionally, in Figure S31 (Supporting Information), it can be seen that these peaks are in plane and that there is a broad band in the out-of-plane direction at $q = 18$ nm^{-1} corresponding to the (001) reflection. This data indicates that the COF-TAPB-BTCA films obtained on the quartz slides and inside our microfluidic device are preferentially oriented with their *c*-axis perpendicular to the

substrate. With this solvent-resistant microfluidic device, we also carried out the synthesis of COF-TAPB-BTCA onto commercially available silicon (111) and single-layer graphene. The COF-TAPB-BTCA films generated showed no differences to the COF-TAPB-BTCA films grown onto quartz (see Figure 4g,h and Figures S32–S34: Supporting Information). Remarkably, COF-TAPB-BTCA samples grown on quartz substrates immersed inside a vial containing the same reaction mixture used for the microfluidic synthesis but where buoyancy-driven convection is not suppressed, exhibited a completely different morphology. As shown in Figure 4j, mixing COF-TAPB-BTCA monomers inside a vial and allowing them to react for 72 h only yields spheres of several hundreds of nanometers. Note that this morphology is typical and well-known in the literature for this type of material when a poor control of the convective transport processes dominates.[30] Therefore, these results clearly confirm that simulated microgravity conditions are not only ideal to control the orientation, compactness and crack-free generation of 2D porous crystalline molecular frameworks, but they can also change their crystal morphogenesis.

3. Conclusions

We have shown an easy way to achieve space-like experimentation conditions on Earth employing a custom-made microfluidic device for the fabrication of 2D crystalline molecular frameworks. The results presented throughout this work confirm that experimentation under simulated microgravity conditions has unprecedented effects on the controlled growth of 2D crystalline molecular frameworks. Homogeneous and large thin films formed by either metal–organic or covalent bonds could be obtained in a wide variety of substrates with a high control on their crystalline orientation. We have proved that these simulated microgravity conditions can open new routes to straightforwardly study properties such as the anisotropy of conductivity in 2D conductive crystalline molecular frameworks. Accordingly, we believe that this work will provide a new "playground" to chemists, physicists and materials scientists that want to generate unprecedented 2D functional materials and devices.

Supporting Information

Supporting Information is available from the Wiley Online Library or from the author.

Acknowledgements

N.C.-P., D.R.-S.-M., C.F. contributed equally to this work. This work was supported by the European Research Council Starting Grant microCrysFact (ERC-2015-STG No. 677020), the Horizon 2020 FETOPEN project SPRINT (No. 801464), the Swiss National Science Foundation (project no. 200021_181988), grant MAT 2015-70615-R from the Spanish Government funds and by the European Regional Development Fund (ERDF). The ICN2 is funded by the CERCA programme/Generalitat de Catalunya. The ICN2 is supported by the Severo Ochoa Centres of Excellence programme, funded by the Spanish Research Agency (AEI, grant no. SEV-2017-0706). N.C.-P. acknowledges support from "laCaixa" Foundation (fellowship ID 100010434). The fellowship code is LCF/BQ/ES17/11600012. N.C.-P. also acknowledges the financial support of COST action MP1407. R.P. acknowledges support from the Marie Curie Cofund, Beatriu de Pinós Fellowship AGAUR 2017 BP 00064. The GIWAXS experiments were conducted on the NCD-SWEET beamline of the ALBA synchrotron, Spain and on the SAXS/WAXS beamline of the Australian Synchrotron, ANSTO, Australia. GIWAXS experiments of $Ni_3(HITP)_2$ and COF-TAPB-BTCA were performed at the NCD-SWEET beamline at ALBA Synchrotron with the collaboration of ALBA staff. The authors acknowledge the support of the ANSTO, in providing the facilities for the GIWAXS experiments used for the characterization of COF-TAPB-BTCA in this work.

Conflict of Interest

The authors declare no conflict of interest.

Data Availability Statement

The data that support the findings of this study are available from the corresponding author upon reasonable request.

Keywords

2D porous crystalline materials, covalent organic frameworks, metal–organic frameworks, microfluidic technologies, simulated microgravity

Received: March 5, 2021
Revised: April 10, 2021
Published online:

[1] A. R. Millward, O. M. Yaghi, *J. Am. Chem. Soc.* **2005**, *127*, 17998.
[2] M. Latroche, S. Surblé, C. Serre, C. Mellot-Draznieks, P. L. Llewellyn, J.-H. Lee, J.-S. Chang, S. H. Jhung, G. Férey, *Angew. Chem., Int. Ed.* **2006**, *45*, 8227.
[3] M. Kandiah, M. H. Nilsen, S. Usseglio, S. Jakobsen, U. Olsbye, M. Tilset, C. Larabi, E. A. Quadrelli, F. Bonino, K. P. Lillerud, *Chem. Mater.* **2010**, *22*, 6632.
[4] S. H. Jhung, J.-H. Lee, J. W. Yoon, C. Serre, G. Férey, J.-S. Chang, *Adv. Mater.* **2007**, *19*, 121.
[5] Z.-G. Gu, S.-C. Chen, W.-Q. Fu, Q. Zheng, J. Zhang, *ACS Appl. Mater. Interfaces* **2017**, *9*, 7259.
[6] B. Sen, J. C. C. Santos, R. Haldar, Q. Zhang, T. Hashem, P. Qin, Y. Li, F. Kirschhöfer, G. Brenner-Weiss, H. Gliemann, L. Heinke, C. Barner-Kowollik, A. Knebel, C. Wöll, *Nanoscale* **2020**, *12*, 24419.
[7] K. Yuan, T. Song, X. Zhu, B. Li, B. Han, L. Zheng, J. Li, X. Zhang, W. Hu, *Small* **2019**, *15*, 1804845.
[8] V. Rubio-Giménez, M. Galbiati, J. Castells-Gil, N. Almora-Barrios, J. Navarro-Sánchez, G. Escorcia-Ariza, M. Mattera, T. Arnold, J. Rawle, S. Tatay, E. Coronado, C. Martí-Gastaldo, *Adv. Mater.* **2018**, *30*, 1704291.
[9] T. Kambe, R. Sakamoto, K. Hoshiko, K. Takada, M. Miyachi, J.-H. Ryu, S. Sasaki, J. Kim, K. Nakazato, M. Takata, H. Nishihara, *J. Am. Chem. Soc.* **2013**, *135*, 2462.
[10] A. McPherson, L. J. DeLucas, *npj Microgravity* **2015**, *1*, 15010.
[11] R. L. Kroes, D. Reiss, *J. Cryst. Growth* **1984**, *69*, 414.
[12] T. Chen, J.-H. Dou, L. Yang, C. Sun, N. J. Libretto, G. Skorupskii, J. T. Miller, M. Dincă, *J. Am. Chem. Soc.* **2020**, *142*, 12367.

[13] R. W. Day, D. K. Bediako, M. Rezaee, L. R. Parent, G. Skorupskii, M. Q. Arguilla, C. H. Hendon, I. Stassen, N. C. Gianneschi, P. Kim, M. Dincă, *ACS Cent. Sci.* **2019**, *5*, 1959.
[14] L. S. Xie, G. Skorupskii, M. Dincă, *Chem. Rev.* **2020**, *120*, 8536.
[15] A. Mähringer, A. C. Jakowetz, J. M. Rotter, B. J. Bohn, J. K. Stolarczyk, J. Feldmann, T. Bein, D. D. Medina, *ACS Nano* **2019**, *13*, 6711.
[16] C. Hu, Y. Bai, M. Hou, Y. Wang, L. Wang, X. Cao, C.-W. Chan, H. Sun, W. Li, J. Ge, K. Ren, *Sci. Adv.* **2020**, *6*, eaax5785.
[17] M. Faustini, J. Kim, G.-Y. Jeong, J. Y. Kim, H. R. Moon, W.-S. Ahn, D.-P. Kim, *J. Am. Chem. Soc.* **2013**, *135*, 14619.
[18] A. Sorrenti, L. Jones, S. Sevim, X. Cao, A. J. DeMello, C. Martí-Gastaldo, J. Puigmartí-Luis, *J. Am. Chem. Soc.* **2020**, *142*, 9372.
[19] D. Sheberla, L. Sun, M. A. Blood-Forsythe, S. Er, C. R. Wade, C. K. Brozek, A. Aspuru-Guzik, M. Dincă, *J. Am. Chem. Soc.* **2014**, *136*, 8859.
[20] M.-S. Yao, X.-J. Lv, Z.-H. Fu, W.-H. Li, W.-H. Deng, G.-D. Wu, G. Xu, *Angew. Chem., Int. Ed.* **2017**, *56*, 16510.
[21] Y. Liu, J. Guo, E. Zhu, L. Liao, S.-J. Lee, M. Ding, I. Shakir, V. Gambin, Y. Huang, X. Duan, *Nature* **2018**, *557*, 696.
[22] M. Farmanbar, G. Brocks, *Adv. Electron. Mater.* **2016**, *2*, 1500405.
[23] Y. Liu, P. Stradins, S.-H. Wei, *Sci. Adv.* **2016**, *2*, 1600069.
[24] V. Rubio-Giménez, N. Almora-Barrios, G. Escorcia-Ariza, M. Galbiati, M. Sessolo, S. Tatay, C. Martí-Gastaldo, *Angew. Chem., Int. Ed.* **2018**, *57*, 15086.
[25] K. S. Krishnan, N. Ganguli, *Nature* **1939**, *144*, 667.
[26] A. K. Dutta, *Phys. Rev.* **1953**, *90*, 187.
[27] O. J. Guentert, C. A. Klein, *Appl. Phys. Lett.* **1963**, *2*, 125.
[28] A. de la Peña Ruigómez, D. Rodríguez-San-Miguel, K. C. Stylianou, M. Cavallini, D. Gentili, F. Liscio, S. Milita, O. M. Roscioni, M. L. Ruiz-González, C. Carbonell, D. Maspoch, R. Mas-Ballesté, J. L. Segura, F. Zamora, *Chem. – Eur. J.* **2015**, *21*, 10666.
[29] B. J. Smith, A. C. Overholts, N. Hwang, W. R. Dichtel, *Chem. Commun.* **2016**, *52*, 3690.
[30] D. Rodríguez-San-Miguel, A. Yazdi, V. Guillerm, J. Pérez-Carvajal, V. Puntes, D. Maspoch, F. Zamora, *Chem. – Eur. J.* **2017**, *23*, 8623.